

Flexible Networks for Learning Physical Dynamics of Deformable Objects

Jinhyung Park,¹ Dohae Lee,¹ In-Kwon Lee¹

¹ Yonsei University

jh9604@yonsei.ac.kr, dlehgo1414@gmail.com, iklee@yonsei.ac.kr

Abstract

Learning the physical dynamics of deformable objects with particle-based representation has been the objective of many computational models in machine learning. While several state-of-the-art models have achieved this objective in simulated environments, most existing models impose a precondition, such that the input is a sequence of ordered point sets - i.e., the order of the points in each point set must be the same across the entire input sequence. This restrains the model to generalize to real-world data, which is considered to be a sequence of unordered point sets. In this paper, we propose a model named *time-wise PointNet* (TP-Net) that solves this problem by directly consuming a sequence of unordered point sets to infer the future state of a deformable object with particle-based representation. Our model consists of a shared feature extractor that extracts global features from each input point set in parallel and a prediction network that aggregates and reasons on these features for future prediction. The key concept of our approach is that we use global features rather than local features to achieve invariance to input permutations and ensure the stability and scalability of our model. Experiments demonstrate that our model achieves state-of-the-art performance in both synthetic dataset and in real-world dataset, with real-time prediction speed. We provide quantitative and qualitative analysis on why our approach is more effective and efficient than existing approaches.

1 Introduction

Humans have the ability to reason on historical trajectories of various objects and easily make inferences on future states based on their intuitions. In order to mimic such ability, developing a computational model that can learn the physical dynamics of objects has been a core domain in computer vision, robotics, and in machine learning (Chen, Billings, and Grant 1990; Wan et al. 2001). To implement such computational models, physical reasoning on objects with particle-based representations has garnered considerable attention in recent years (Macklin et al. 2014). As particle-based representations provide flexibility in representing objects with complex shapes, several studies have provided frameworks that can learn the physical dynamics of deformable objects with particle-based representation (Mrowca et al. 2018; Li et al. 2019b, 2020).

While these models have achieved state-of-the-art performance in predicting the future state of deformable objects,

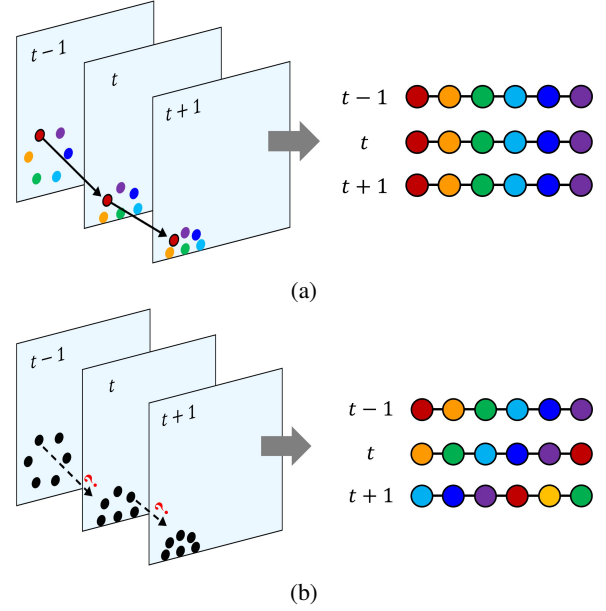


Figure 1: (a) We can easily configure a sequence of ordered point sets in simulated environments. (b) The previous condition is seldom met in real-world.

these models are optimized from learning a *sequence of ordered point sets*. In other words, the order of the points in each point set in the sequence must be the same across the entire sequence, when training or testing the model. One of the reasons for imposing this precondition in the data is to use a weight-shared LSTM (Hochreiter and Schmidhuber 1997) layer in the model architecture or to reason on the historical trajectories of individual points easily. However, this approach is only feasible in simulated environments where we can map each point in the current frame to its corresponding point in the previous frame (Figure 1a). In real-world, individual point correspondences between different frames are not observable, thus making it challenging to configure a sequence of ordered point sets (Figure 1b). Although sorting the points in each frame into a canonical order might seem to resolve this problem, PointNet (Qi et al. 2017) demonstrates that in high-dimensional space, there exists no ordering that

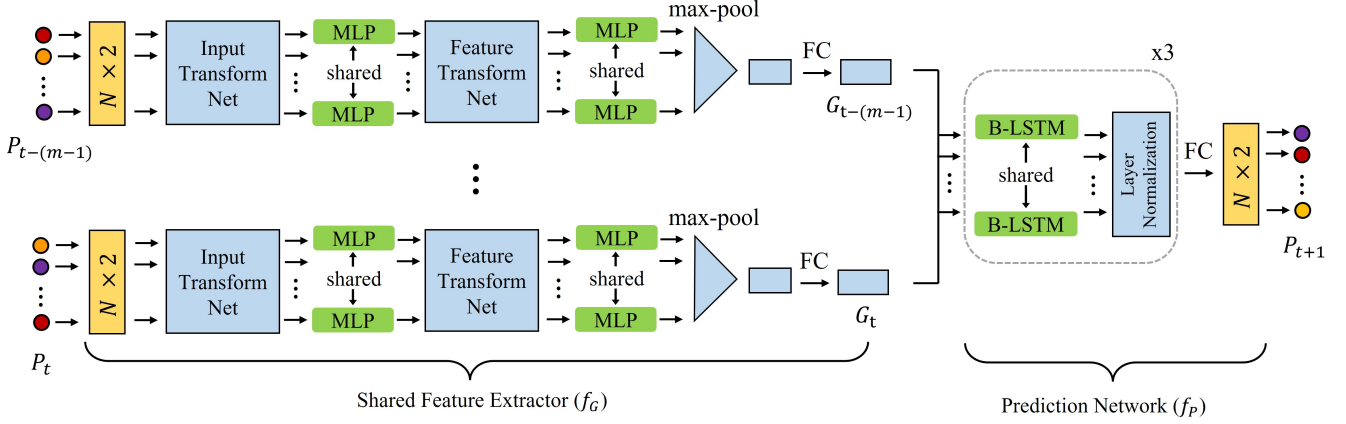


Figure 2: TP-Net Architecture. The network takes a sequence of m unordered point sets as input, and outputs the predicted unordered point set in the next time step. “MLP”, “FC” and “B-LSTM” stands for multi-layer perceptron, fully-connected layer and bidirectional-LSTM layer, respectively. The input transform net and feature transform net is directly adopted from the existing classification network – PointNet.

is stable with respect to point perturbations.

In order to build a flexible neural network that is independent of this concern, we propose a model named *time-wise PointNet* (TP-Net) that can directly consume a sequence of unordered point sets to infer the future dynamics of a deformable object. The proposed model extends the key concept of an existing classification network called PointNet (Qi et al. 2017), and achieves invariance to $(N!)^m$ input permutations, where N and m denote the number of points in each point set and the number of point sets in the sequence that the model takes as input, respectively. In Section 3, we demonstrate how our model achieves this property and explain why extending the key idea from a classification network to design a time-series model for physical reasoning is an effective approach. The results from our experiments indicate that TP-Net outperforms existing models including state-of-the-art, in predicting the future state of both simulated and real-world deformable objects, with $O(N)$ time and space complexity.

The key contributions of our work are as follows:

- We design a deep neural network that can directly consume a sequence of unordered point sets to predict the future particle positions of simulated and real-world deformable objects;
- Based on qualitative and quantitative analyses, we show how the key idea from an existing classification network can be extended to develop an effective time-series model for physical reasoning;
- We demonstrate the efficiency of our approach compared to existing approaches for consuming a sequence of unordered point sets, based on theoretical and empirical analyses.

2 Related Work

Physical Reasoning on N-Body System An early attempt to develop a learnable physics engine that can reason on in-

teracting objects was achieved by the interaction network (Battaglia et al. 2016). The interaction network showed the effectiveness of utilizing graph neural networks (GNN) (Scarselli et al. 2008) for physical reasoning on systems with N bodies, which inspired several other studies to propose learnable simulators based on GNN (Cranmer et al. 2020; Kipf et al. 2018; Graber and Schwing 2020; Webb et al. 2019; Li et al. 2019a; Martinkus, Lucchi, and Perraudin 2021). These approaches have in common that for each time step, the system is represented as a graph where each node and edge represents an object and the relationship between objects, respectively. By updating the state of each node over time by message-passing (Duvenaud et al. 2015), the network can learn to infer the future state of each node, based on relational reasoning (Santoro et al. 2017) and relational inductive bias (Battaglia et al. 2018).

Recently, dNRI (Graber and Schwing 2020) and NRI (Kipf et al. 2018) have demonstrated its effectiveness in using GNN to predict the interactions between particles purely from observational data. These approaches are also applicable in predicting the future state of a deformable object that is modeled with mass-spring system. However, these models can only learn to predict the future from a sequence of ordered point sets. Although a graph for each time step can be constructed from an unordered point set since a graph is invariant to input permutations of the nodes, the order of the points matters when reasoning on two different graphs. For example, if the input point set at time steps t and $t + 1$ are given as $\{(x_1^t, y_1^t), (x_2^t, y_2^t), (x_3^t, y_3^t)\}$ and $\{(x_2^{t+1}, y_2^{t+1}), (x_1^{t+1}, y_1^{t+1}), (x_3^{t+1}, y_3^{t+1})\}$, respectively, the network learns a message-passing function based on the assumption that (x_1, y_1) , (x_2, y_2) , and (x_3, y_3) changes to (x_2^{t+1}, y_2^{t+1}) , (x_1^{t+1}, y_1^{t+1}) , and (x_3^{t+1}, y_3^{t+1}) , respectively. Therefore, training or testing the network with misaligned point set sequences results in inferior performances, thus restraining the model to generalize to real-world data where a sequence of ordered point sets is not configurable. We em-

pirically prove such behavior in Section 4.2.

Physical Reasoning on Deformable Objects Similar approaches of utilizing GNN were adopted to develop a learnable simulator for deformable objects (Mrowca et al. 2018; Li et al. 2019b, 2020; Sanchez-Gonzalez et al. 2020). In these studies, deformable objects are modeled with a particle-based representation and future predictions were made on individual particles, based on the learned physical dynamics of the system. These approaches showed excellent performance in inferring the future dynamics of simulated deformable objects, yet they assume a few conditions that are seldom met in practice. In addition to the assumption that the input is a sequence of ordered point sets, the hierarchical relation network (Mrowca et al. 2018) and dynamics prior (Li et al. 2019b, 2020) require relational attributes as input, which describes the relationship between individual particles in the system. Since relational attributes are not observable in many real-world scenarios, the model lacks generalization ability and shows inferior performance without those attributes, as we show this behavior in Section 4.

Consuming Sequence of Unordered Point Sets While our method of consuming a sequence of unordered point sets fundamentally differs from existing approaches, a few studies have also proposed networks that can process a sequence of unordered point sets for various purposes (Min et al. 2020; Fan and Yang 2019; Gomes, Rossi, and Toni 2021; Liu, Yan, and Bohg 2019). The key idea common in these approaches is that for each point in the current frame, the network searches for k-nearest-neighbors or relevant points in the previous frame. By combining state information of neighboring points in the past, the model achieves permutation invariance while preserving the spatial structure of the input. While this approach showed state-of-the-art performance in gesture recognition, such method shows poor performance when applied in future prediction (see results of GraphRNN in Section 4.1). As the network significantly depends on local features and neighbor points of each point, it suffers from serious performance degradation when outlier or unseen points exist in the input, which is a common scenario in long-term prediction. In addition, finding spatio-temporal neighbor points for every point in the point set is a $O(N^2)$ operation – quadratic to the number of input points – that is computationally expensive and lacks scalability to systems with larger particle counts.

3 Method

We define an unordered point set with N points at time t as $P_t = \{p_{1,t}, p_{2,t}, \dots, p_{N,t}\}$ with $p_{i,t} \in \mathbb{R}^2$ being the Euclidean coordinates of point i in P_t . Then, we formulate our problem by learning a continuous function f that infers the future point set P_{t+1} of a deformable object modeled with mass-spring system, when a sequence of m unordered point sets is given as the context:

$$P_{t+1} = f(P_{t-(m-1)}, P_{t-(m-2)}, \dots, P_{t-1}, P_t). \quad (1)$$

3.1 Model Overview

To develop a framework that can process a sequence of unordered point sets for physical reasoning, we propose our model called TP-Net, which has two key modules: shared feature extractor and prediction network (Figure 2). The key idea of our model is that we aggregate global features of each point set to predict individual particle positions in the next time step. In addition to making TP-Net invariant to $(N!)^m$ input permutations, this approach is also robust to input perturbations and outliers, thereby facilitating stable long-term predictions, especially in predicting the shape deformation of the object. We explain how TP-Net achieves these objectives in the following section and demonstrate its effectiveness in Section 4.

3.2 Shared Feature Extractor

We first design our shared feature extractor that learns a continuous set function f_G , which takes a single unordered point set P_t as input and outputs global features G_t (Equation (4)). Then, we apply this to each one of m input point sets in parallel. This process can be represented by the following equations:

$$G_{t-(m-1)} = f_G(P_{t-(m-1)}), \quad (2)$$

...

$$G_{t-1} = f_G(P_{t-1}), \quad (3)$$

$$G_t = f_G(P_t). \quad (4)$$

Since the global features extracted from each input point set are invariant to $N!$ input permutations (the order of the points in the input point set), we achieve invariance to $(N!)^m$ input permutations in total since we extract global features from m input point sets independently. While global features G_t are invariant to the order of the points in the input point set, we define global features G_t as a *sequence* of features:

$$G_t = (g_1^t, g_2^t, \dots, g_k^t), \quad (5)$$

where g_i^t is the i -th feature of the point set P_t , and k is the number of features we encode from a point set. The purpose of defining global features as a *sequence* of features rather than a *set* of features, is to align the same type of features of each point set when we aggregate multiple global features $G_{t-(m-1)}, \dots, G_{t-1}, G_t$ in the prediction network. This allows the prediction network to apply a weight-shared LSTM layer on these aligned global features.

Implementation Details Our shared feature extractor adopts a submodule of the classification network from PointNet (Qi et al. 2017). The classification network from PointNet takes a single unordered point set as input and outputs the predicted score of each class to perform object classification. While we use the same structure of this network to design our shared feature extractor, we modify the last part of the network to output global features. We also adjust the input vector shape and layer sizes to process 2D data (instead of 3D data) as we use 2D datasets (Figure 2).

The network first applies a series of shared MLP layers on each point independently for input transformations, feature transformations, and local features extraction. Then, the

network aggregates per point features by max pooling to extract global features of the point set. Although the original PointNet applies another series of MLP layers and a softmax function on these global features, our network applies a single MLP layer and a ReLU function on these global features instead, to extract the final global features as output.

Extending PointNet for Future Prediction Although PointNet is originally designed to capture relevant features for classification or semantic segmentation, PointNet is an excellent source for future frame prediction of deformable objects with particle-based representation. PointNet learns a continuous set function that summarizes a shape into a sparse set of key points. Since the global features extracted from the PointNet are bottleneck features of these key points, these features are robust to small perturbation or outliers in the input. Therefore, we extract global features from each point set in parallel and predict the future particle positions by reasoning on these global features sequentially with the expectation that our model will be robust to outliers during prediction rollout. In Section 4, we show this behavior of TP-Net and prove its effectiveness.

3.3 Prediction Network

The prediction network learns a continuous function f_P , that uses global features extracted from each input point set to predict the future particle positions P_{t+1} :

$$P_{t+1} = f_P(G_{t-(m-1)}, \dots, G_{t-1}, G_t). \quad (6)$$

Implementation Details We implement our prediction network by first aggregating the global features $G_{t-(m-1)}, \dots, G_{t-1}, G_t$ into a sequence of global features \mathcal{G} :

$$\mathcal{G} = (G_{t-(m-1)}, \dots, G_{t-1}, G_t), \quad (7)$$

to preserve the temporal structure of the original input. Note that global features per every time step are also another *sequence* of features as illustrated in Equation (5). Since we apply the same shared feature extractor to all input point set in parallel, the order of the features in every global features is the same – i.e., $G_i = (g_1^i, g_2^i, \dots, g_k^i)$ for all $i = t - (m - 1), \dots, t - 1, t$. Since \mathcal{G} maintains the same order of features in G_i across the entire sequence, we then apply a bidirectional LSTM layer to \mathcal{G} with the assumption that each feature g_j^t has an independent hidden state h_j^t and a cell state c_j^t :

$$h_j^t, c_j^t = \text{LSTM}(g_j^t, h_j^t, c_j^t). \quad (8)$$

After we apply three bidirectional LSTM layers (with layer normalization (Ba, Kiros, and Hinton 2016) in between bidirectional LSTM layers), we apply a fully-connected layer and reshape the output into a 2D point set (Figure 2).

3.4 Model Training

Dataset We first train and test our model on a synthetic dataset of moving deformable object with particle-based representation. Then, we directly test our model on real-world dataset that is similar to the synthetic dataset in terms of object radius, velocity and rigidity.

For synthetic dataset, we use the Box2D physics engine (Catto 2020) to generate 7125 simulated trajectories of a deformable object. We model our deformable object with a mass-spring system where 30 particles comprises the boundary of the object and each particle is jointly connected to a number of other particles by a restorable spring. When generating the simulated trajectories, we randomize the initial position, initial force and initial direction of the object.

For real-world dataset, we capture 40 trajectories of a real-world deformable object by using a high speed camera. Then, we preprocess the video data to construct a sequence of unordered point sets that represents the trajectory of the deformable object (refer to the data appendix for detail).

Loss Function and Hyperparameters We define our loss function L_{CD} by using the Chamfer distance (Barrow et al. 1977) between the ground truth point set P and the predicted point set \hat{P} :

$$L_{CD}(P, \hat{P}) = \sum_{x \in P} \min_{y \in \hat{P}} \|x - y\|_2^2 + \sum_{y \in \hat{P}} \min_{x \in P} \|x - y\|_2^2. \quad (9)$$

In order to increase the long-term prediction ability of our model along with robustness to input perturbations, we make our model to recursively predict eight future point sets during training. Thus, we define our final loss L as the sum of losses of each predicted point set:

$$L = \sum_{i=1}^8 w_i L_{CD}(P_{t+i}, \hat{P}_{t+i}), \quad (10)$$

where $w_1 = 9$ and $w_i = 1$ for all $i = 2, 3, \dots, 8$ to balance the weight of predicting future point sets when a clean input is given and when input with noise is given.

When training our model, we use a learning rate of 10^{-3} with the Adam optimizer (Kingma and Ba 2015) and train it for 100 epochs with a batch size of 128 on Intel(R) Core(TM) i5-8400 CPU @ 2.80Hz and GeForce GTX1080 Ti for 18 to 24 hours.

4 Experiment

We study our framework using two datasets: synthetic dataset and real-world dataset. For each dataset, we quantitatively and qualitatively compare the performance of TP-Net with other benchmarks – dNRI (Graber and Schwing 2020), StaticNRI/DynamicNRI (Kipf et al. 2018), DynamicsPrior (Li et al. 2019b,b), and GraphRNN (Gomes, Rossi, and Toni 2021) – that are capable of predicting the future state of a deformable object. Then, we analyze and compare the time and space complexity of our model against GraphRNN.

Evaluation Metrics For all experiments, we quantitatively measure the rollout error in two aspects – position error and shape error. We first define the position error E_p as the average Chamfer distance between the ground truth point set P and the predicted point set \hat{P} :

$$E_p(P, \hat{P}) = \frac{1}{|P|} \left(\sum_{x \in P} \min_{y \in \hat{P}} \|x - y\|_2^2 + \sum_{y \in \hat{P}} \min_{x \in P} \|x - y\|_2^2 \right). \quad (11)$$

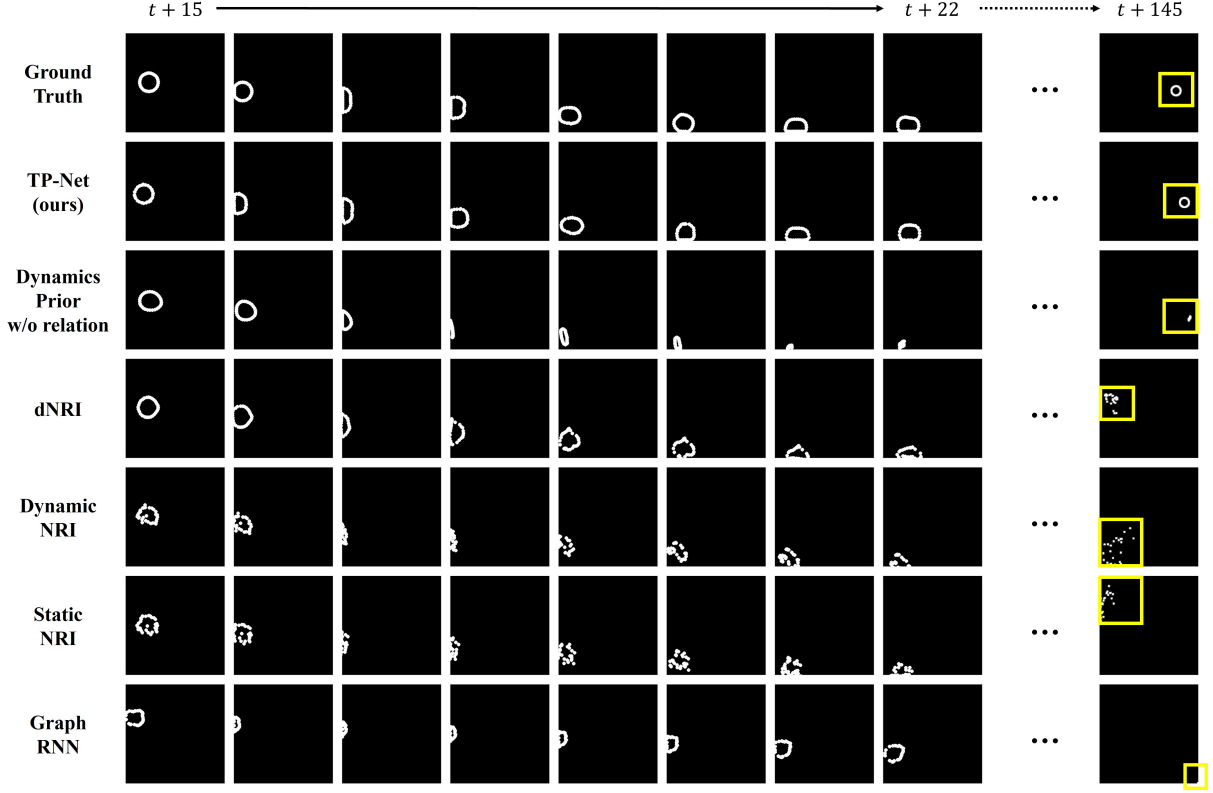


Figure 3: Future prediction on moving deformable object (synthetic dataset). We visualize the prediction results after 15 to 22 time steps and after 145 time steps when five input frames are initially given. For the eight output frames from $t + 15$ to $t + 22$, we zoom-in the left-bottom quadrant of the frame. For the output frame at $t + 145$, we draw a yellow bounding box to locate the deformable object in the frame.

However, the average Chamfer distance cannot fully reflect the shape difference between two point sets, as it simply measures the positional difference between individual particles (refer to the appendix for details). Therefore, we define the shape error E_s by using a variation of the vanilla Chamfer distance. We first apply a translation matrix to each point set, such that the center of each point set can be translated to the origin. Then, we compute the average Chamfer distance on these translated point sets. The equation for computing the shape error is as follows:

$$E_s(P, \hat{P}) = E_p(M_c P, M_{\hat{c}} \hat{P}), \quad (12)$$

where c is the center of mass of P , \hat{c} is the center of mass of \hat{P} , M_c is a translation matrix that translates x to $x - c_x$ and y to $y - c_y$, and $M_{\hat{c}}$ is a translation matrix that translates x to $x - \hat{c}_x$ and y to $y - \hat{c}_y$. In this way, we directly compare the geometric shape of two point sets regardless of their relative positions in the Euclidean space.

Environments We train each model on the synthetic dataset three times with different input conditions – giving three, four, and five input frames. Although our model TP-Net and GraphRNN can process both sequences of unordered and ordered point sets, we train and evaluate each model by solely using sequences of ordered point sets from

the synthetic dataset to respect the precondition of the input for dNRI, StaticNRI, DynamicNRI, and DynamicsPrior. Moreover, we only use the position data for the input when training and evaluating each model, since other attributes are difficult to obtain from real-world data. Therefore, we zero pad the relation attribute in the input when training and testing DynamicsPrior, and we use the positional difference along the time steps as the velocity attribute when training dNRI, StaticNRI, and DynamicNRI.

4.1 Synthetic Dataset

Qualitative Comparison We test each model and visualize the predicted points along with the ground truth for qualitative comparison. As illustrated in Figure 3, TP-Net is the only model that well predicts both the future trajectory and shape deformation of the object. Generally, all other models except TP-Net show significant performance degradation after 1st or 2nd collision of the object. While DynamicsPrior can predict the future trajectory of the object with high accuracy even in long term prediction, TP-Net significantly outperforms DynamicsPrior in predicting the shape deformation. This proves the effectiveness of our approach – using max-pooled global features to predict the future state of each particles. Although TP-Net intermittently generates an outlier during the rollout, the model selects informative fea-

Table 1: Average rollout error of future prediction on moving deformable object (synthetic dataset). CD indicates the position error (Chamfer distance) and CD* indicates the shape error (variation of the vanilla Chamfer distance) of each model. The asteroid(*) next to DynamicsPrior denotes that the model is trained and tested without relation attribute.

| Prediction Steps | # input frames = 3 | | | | # input frames = 4 | | | | # input frames = 5 | | | |
|------------------|--------------------|--------------|--------------|--------------|--------------------|--------------|--------------|--------------|--------------------|--------------|--------------|--------------|
| | 40 | | 80 | | 40 | | 80 | | 40 | | 80 | |
| Rollout Error | CD | CD* | CD | CD* | CD | CD* | CD | CD* | CD | CD* | CD | CD* |
| TP-Net (ours) | 0.094 | 0.007 | 0.246 | 0.007 | 0.071 | 0.007 | 0.164 | 0.007 | 0.101 | 0.008 | 0.225 | 0.007 |
| DynamicsPrior* | 0.110 | 0.044 | 0.252 | 0.050 | 0.074 | 0.040 | 0.186 | 0.046 | 0.116 | 0.041 | 0.231 | 0.064 |
| dNRI | 0.291 | 0.031 | 0.867 | 0.055 | 0.092 | 0.024 | 0.882 | 0.046 | 0.106 | 0.022 | 0.613 | 0.035 |
| DynamicNRI | 0.788 | 0.113 | 0.760 | 0.292 | 0.313 | 0.036 | 0.946 | 0.047 | 0.254 | 0.031 | 0.882 | 0.044 |
| StaticNRI | 0.668 | 0.143 | 0.714 | 0.286 | 0.312 | 0.036 | 0.946 | 0.047 | 0.254 | 0.031 | 0.882 | 0.044 |
| GraphRNN | 1.235 | 0.055 | 2.398 | 0.069 | 0.370 | 0.030 | 0.699 | 0.054 | 0.342 | 0.024 | 1.154 | 0.092 |

tures from the point set and corrects those outliers in the next time step, thus maintaining reasonable shape of the object in long term. Conversely, model that uses neighboring points or local structures to predict the future state of each points, e.g., GraphRNN, shows significantly inferior performance in long-term prediction.

Quantitative Comparison We also evaluate and compare the performance by using quantitative metrics. We compute the average rollout error on 60 simulated trajectories of a deformable object, and compare its value after 40 and 80 time steps, respectively. As presented in Table 1, our model TP-Net achieves state-of-the-art performance in terms of both metrics – position error and shape error. Although DynamicsPrior shows as high performance as TP-Net in terms of position error, the metric needs additional interpretation. As illustrated in Figure 3, DynamicsPrior is simply good at predicting the general trajectory of individual particles without reasoning on its geometric shape, which could still result in low position error by figure. In fact, TP-Net not only outperforms DynamicsPrior by a large margin (6-9 times) in terms of shape error, but also maintains a relatively constant shape error even in long term prediction.

Moreover, note that the analysis above is based on the results when each model is trained and tested solely on sequences of ordered point sets. Therefore, training and testing each model on sequences of unordered point sets will result in inferior performances for dNRI, StaticNRI, DynamicNRI, and DynamicsPrior which depends on the order of the points in each input point set.

4.2 Real world Dataset

Generalization to Real World Data To demonstrate the generalization ability of TP-Net to real-world scenarios, we test our learned model directly on real-world dataset. Since we cannot configure a sequence of ordered point sets for input in this time, we arbitrarily configure the order of the points in each input frame and validate our model’s ability in processing a sequence of unordered point sets.

We give five steps of particle positions as input and make our model to predict the future particle positions until the object disappears from the scene. The results illustrated in Figure 4 shows that the learned policy of our model shows

great potential to generalize to real world. Without knowing any information of the point correspondences between different input frames, TP-Net can reason on the underlying physical dynamics and infer the future state of a real world deformable object with reasonable accuracy.

Comparison to Other Works We also compare the generalization ability of TP-Net to other benchmarks. To test the robustness of each model to different input ordering methods, we test each model on each test case with three different kinds of input. The three different input ordering method we use are as follows: (1) Sorting the points in each input frame in ascending x positions, (2) sorting the points in each input frame in descending y positions, and (3) randomly shuffling the order of the points in each input frame.

We evaluate the rollout error on 40 trajectories of real-world deformable objects when three input frames are given. Figure 5 shows that TP-Net outperforms all other benchmarks in terms of both metrics and for all kinds of input ordering methods. It is not surprising that TP-Net and GraphRNN shows constant performance regardless of the input ordering method as they are invariant to input permutations. However, TP-Net outperforms GraphRNN by a large margin in both metrics, which demonstrates the effectiveness of our approach in processing a sequence of unordered point sets. For other models, the performance fluctuates depending on the input ordering method, but there exists no ordering that results in the best performance for all models, or results in higher performance than TP-Net. Although we have only tried three methods of input ordering, these results imply that there exists no ordering of a point set that ensures stable performance in the general sense, thus demonstrating the importance of achieving permutation invariance, again.

4.3 Time and Space Complexity Analysis

In this section, we compare the time and space complexity of TP-Net and GraphRNN (Gomes, Rossi, and Toni 2021) which are both capable of processing a sequence of unordered point sets for future prediction.

Table 2 shows the time complexity – number of floating-point operations per sample (FLOPs/sample) – and space complexity – number of parameters in the network (#params) – of TP-Net and GraphRNN. While GraphRNN

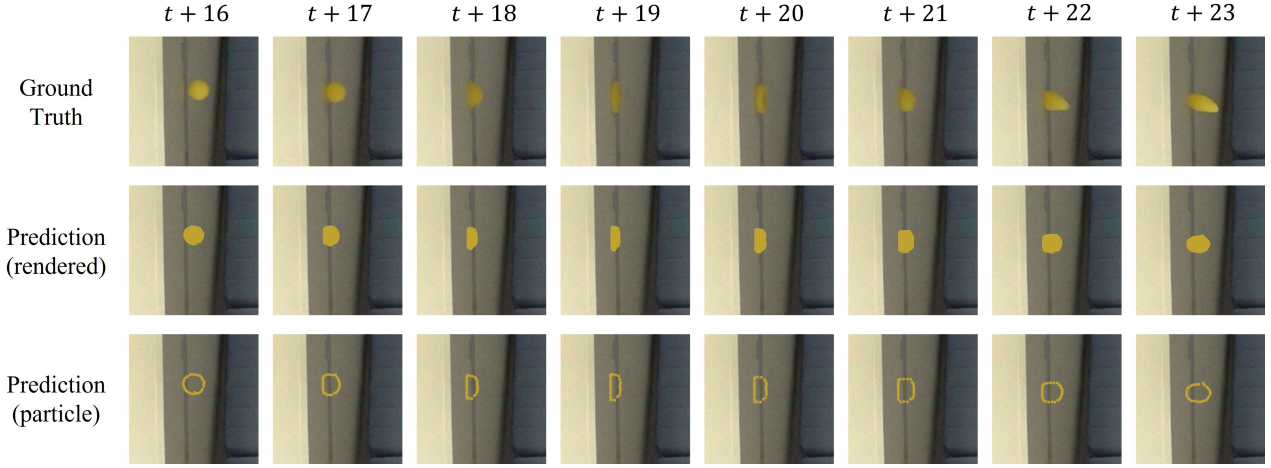
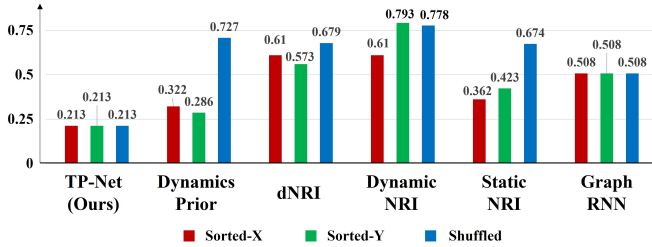
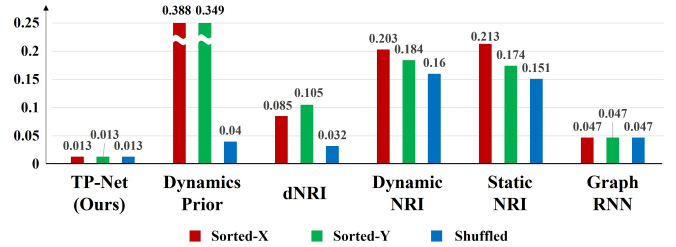


Figure 4: Future predictions on real deformable object. The images in the first row are the original frames from the camera. The images in the bottom row are generated by plotting the predicted positions of each particle in the background image. The images in the middle row are generated by painting the interior of the contour drawn by connecting the predicted particles.



(a) Average position error of future prediction on real-world data



(b) Average shape error of future prediction on real-world data

Figure 5: For each model, we measure the rollout error after 40 time steps of each scenario with different input ordering method.

is more space efficient than TP-Net in terms of #params in the network (18.75 times less parameters), TP-Net is significantly more efficient in computational cost as it has 354.4 times less floating point operations per sample. As described in Section 2, the time complexity of GraphRNN is $O(N^2)$ – quadratic in the number of points – because it searches for spatio-temporal neighbor points for every point in the current frame. However, the time and space complexity of TP-Net is $O(N)$ since it simply extracts global features from each point set by max pooling per point features, and reasons on those global features sequentially, thus making our approach more scalable than existing methods. Empirically, TP-Net can predict more than 120 future point sets per second on our real-world dataset with a GTX 1080Ti GPU on Tensorflow. Based on these results, we believe our framework can be widely used in real-time applications.

5 Conclusion

We presented a deep neural network named TP-Net that can directly consume a sequence of unordered point sets to infer the future dynamics of a deformable object. By using global features of each point set, our model achieves invariance to $(N!)^m$ input permutations and shows state-of-the-art performance, even in long term prediction. We also demonstrated

Table 2: Time and space complexity of deep architectures for processing a sequence of three unordered point sets with 30 particles. The “M” stands for million.

| | FLOPs/sample | #params |
|---------------|--------------|---------|
| TP-Net (ours) | 21.4M | 7.5M |
| GraphRNN | 7584.6M | 0.4M |

that our model well generalizes to real-world scenarios and is much more efficient than existing methods of consuming a sequence of unordered point sets.

Although we have only used a 2D dataset in this study, in principle, our framework easily generalizes to datasets with higher dimensions, yet additional experiments are needed for verification. Moreover, while here we focused on consuming a sequence of static point sets, many situations involve reasoning on dynamic point sets, where the number of points change over time. Further work is needed to extend our network with more flexibility.

Acknowledgements

This research was supported by the MSIT(Ministry of Science and ICT), Korea, under the ITRC(Information Technology Research Center) support program(IITP-2021-2018-0-01419) supervised by the IITP(Institute for Information and Communications Technology Planning and Evaluation) and the National Research Foundation of Korea(NRF) grant funded by the Korea government(MSIT). (No. NRF-2020R1A2C2014622)

References

- Ba, J. L.; Kiros, J. R.; and Hinton, G. E. 2016. Layer normalization. *arXiv preprint arXiv:1607.06450*.
- Barrow, H. G.; Tenenbaum, J. M.; Bolles, R. C.; and Wolf, H. C. 1977. Parametric correspondence and chamfer matching: Two new techniques for image matching. Technical report, SRI INTERNATIONAL MENLO PARK CA ARTIFICIAL INTELLIGENCE CENTER.
- Battaglia, P. W.; Hamrick, J. B.; Bapst, V.; Sanchez-Gonzalez, A.; Zambaldi, V.; Malinowski, M.; Tacchetti, A.; Raposo, D.; Santoro, A.; Faulkner, R.; et al. 2018. Relational inductive biases, deep learning, and graph networks. *arXiv preprint arXiv:1806.01261*.
- Battaglia, P. W.; Pascanu, R.; Lai, M.; Rezende, D.; and Kavukcuoglu, K. 2016. Interaction networks for learning about objects, relations and physics. *Advances in Neural Information Processing Systems*.
- Catto, E. 2020. Box2D: A 2D Physics Engine for Games.
- Chen, S.; Billings, S. A.; and Grant, P. 1990. Non-linear system identification using neural networks. *International Journal of Control*, 51(6): 1191–1214.
- Cranmer, M.; Sanchez-Gonzalez, A.; Battaglia, P.; Xu, R.; Cranmer, K.; Spergel, D.; and Ho, S. 2020. Discovering symbolic models from deep learning with inductive biases.
- Duvenaud, D.; Maclaurin, D.; Aguilera-Iparraguirre, J.; Gómez-Bombarelli, R.; Hirzel, T.; Aspuru-Guzik, A.; and Adams, R. P. 2015. Convolutional networks on graphs for learning molecular fingerprints. 2224–2232.
- Fan, H.; and Yang, Y. 2019. PointRNN: Point Recurrent Neural Network for Moving Point Cloud Processing. *arXiv*, 1910.08287.
- Gomes, P.; Rossi, S.; and Toni, L. 2021. Spatio-temporal Graph-RNN for Point Cloud Prediction.
- Graber, C.; and Schwing, A. 2020. Dynamic Neural Relational Inference. In *Proceedings of the IEEE/CVF Conference on Computer Vision and Pattern Recognition*.
- Hochreiter, S.; and Schmidhuber, J. 1997. Long short-term memory. *Neural Computation*, 9(8): 1735–1780.
- Kingma, D. P.; and Ba, J. 2015. Adam: A Method for Stochastic Optimization. In *International Conference on Learning Representations*.
- Kipf, T.; Fetaya, E.; Wang, K.-C.; Welling, M.; and Zemel, R. 2018. Neural Relational Inference for Interacting Systems. *International Conference on Machine Learning*.
- Li, Y.; Lin, T.; Yi, K.; Bear, D.; Yamins, D. L.; Wu, J.; Tenenbaum, J. B.; and Torralba, A. 2020. Visual Grounding of Learned Physical Models. In *International Conference on Machine Learning*.
- Li, Y.; Meng, C.; Shahabi, C.; and Liu, Y. 2019a. Structure-informed graph auto-encoder for relational inference and simulation. In *International Conference on Machine Learning Workshop on Learning and Reasoning with Graph-Structured Representations*.
- Li, Y.; Wu, J.; Tedrake, R.; Tenenbaum, J. B.; and Torralba, A. 2019b. Learning Particle Dynamics for Manipulating Rigid Bodies, Deformable Objects, and Fluids. In *International Conference on Learning Representations*.
- Liu, X.; Yan, M.; and Bohg, J. 2019. MeteorNet: Deep Learning on Dynamic 3D Point Cloud Sequences. In *ICCV*.
- Macklin, M.; Müller, M.; Chentanez, N.; and Kim, T.-Y. 2014. Unified particle physics for real-time applications. *ACM Transactions on Graphics (TOG)*, 33(4): 1–12.
- Martinkus, K.; Lucchi, A.; and Perraudin, N. 2021. Scalable Graph Networks for Particle Simulations. *Proceedings of the AAAI Conference on Artificial Intelligence*, 35(10): 8912–8920.
- Min, Y.; Zhang, Y.; Chai, X.; and Chen, X. 2020. An Efficient PointLSTM for Point Clouds Based Gesture Recognition. In *Proceedings of the IEEE/CVF Conference on Computer Vision and Pattern Recognition*, 5761–5770.
- Mrowca, D.; Zhuang, C.; Wang, E.; Haber, N.; Fei-Fei, L.; Tenenbaum, J. B.; and Yamins, D. L. 2018. Flexible Neural Representation for Physics Prediction. In *Advances in Neural Information Processing Systems*.
- Qi, C. R.; Su, H.; Mo, K.; and Guibas, L. J. 2017. Pointnet: Deep learning on point sets for 3d classification and segmentation. In *Proceedings of the IEEE/CVF Conference on Computer Vision and Pattern Recognition*, 652–660.
- Sanchez-Gonzalez, A.; Godwin, J.; Pfaff, T.; Ying, R.; Leskovec, J.; and Battaglia, P. 2020. Learning to simulate complex physics with graph networks. In *International Conference on Machine Learning*, 8459–8468. PMLR.
- Santoro, A.; Raposo, D.; Barrett, D. G.; Malinowski, M.; Pascanu, R.; Battaglia, P.; and Lillicrap, T. 2017. A simple neural network module for relational reasoning. In *Advances in Neural Information Processing Systems*, volume 30, 4967–4976. Curran Associates, Inc.
- Scarselli, F.; Gori, M.; Tsoi, A. C.; Hagenbuchner, M.; and Monfardini, G. 2008. The graph neural network model. *IEEE Transactions on Neural Networks*, 20(1): 61–80.
- Wan, E.; Baptista, A.; Carlsson, M.; Kiebutz, R.; Zhang, Y.; and Bogdanov, A. 2001. Model predictive neural control of a high-fidelity helicopter model. In *AIAA Guidance, Navigation, and Control Conference and Exhibit*, 4164.
- Webb, E.; Day, B.; Andres-Terre, H.; and Lió, P. 2019. Factorised neural relational inference for multi-interaction systems. In *International Conference on Machine Learning Workshop on Learning and Reasoning with Graph-Structured Representations*.

Appendices

A Data Generation

A.1 Synthetic Data

Formulating Deformable Object In this section, we describe how we formulate a deformable object when generating the synthetic dataset with Box2D physics engine (Catto 2020). As illustrated in Figure 6, we model a deformable object with mass-spring system, that has n particles $P = \{p_1, p_2, \dots, p_n\}$ comprising its boundary. For every particle pair (p_i, p_j) that is $|i - j| < \frac{2}{5}n$, we connect the particles with a restorable spring that shares the same spring constant across all springs within the object. In order to mimic the movement of a real-world deformable object we use to generate our real-world dataset, we configure the Box2D environment as follows:

- $n = 30$,
- gravity = (0, -0.5),
- friction of each particle = 1,
- friction of the wall = 1,
- frequency of the spring = 1,
- damping ratio of the spring = 0,
- restitution of each particle = 0,
- restitution of the wall = 1.

Data preparation After we model a deformable object in a 2D Euclidean space, we generate 7125 simulated trajectories of a deformable object such that each trajectory is a sequence of 600 point sets. When generating simulated trajectories, we randomize the initial position, initial force, and initial direction of the object. The scope of randomizing each property is as follows:

- initial force = $\{1.0, 1.15, 1.3, 1.45, 1.6\}$,
- initial direction = $\{180^\circ, 185^\circ, 190^\circ, \dots, 270^\circ\}$,
- initial center position = $\{(x, y) \mid 2.9 \leq x, y \leq 42.1\}$.

After we generate 7125 simulated trajectories, we construct our training dataset and validation dataset by sampling sub-sequences from each trajectory. Each sub-sequence is a sequence of 11 or 12 or 13 point sets, depending on the number of input frames which varies from three to five point sets. For 240 trajectories, we set the entire trajectory as the training scope, and for 6635 trajectories, we only sample sub-sequences from certain parts to construct our training dataset. The rest of the trajectories are used to generate the validation dataset and test dataset. In order to increase the prediction accuracy of our model, especially in terms of predicting the shape deformation of the object, for each trajectory, we sample 15 sub-sequences that involves the interval in which the object collides with the wall, and sample 5 sub-sequences from a normal interval in the trajectory.

We also normalize the position data of each points to be between 0 and 1 when training, and we denormalize the data back to its original value when we visualize the results.

When generating our test set, we generate 60 simulated trajectories with a unique pair of initial force, initial angle,

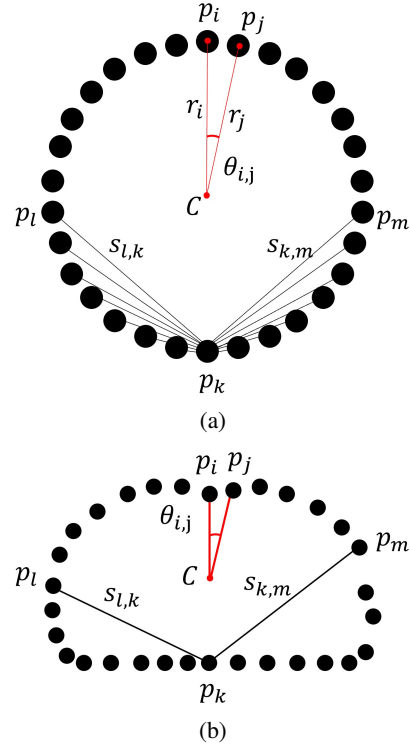


Figure 6: A simplified diagram describing the formulation of a deformable object in Box2D physics engine. (a) In rest state, the distances r_i between the center C of the object and each point p_i are set to two for all $i = 1, \dots, n$. We also connect p_l and p_k with a restorable spring $s_{l,k}$ for all $|l - k| < \frac{2}{5}n$. However, for simplicity, we omit the spring connections that exist in the deformable object in this figure. We also set $\theta_{i,j} = \frac{2\pi}{n}$ for all $i, j \in \{1, \dots, n\}$, which denotes the angle between neighboring points with respect to the center of the object. (b) Spring connections between particles allow deformation of the object.

and initial position, that the model was never trained on, to test the generalization ability of our model.

A.2 Real-World Data

Generating Real-World Trajectories Due to the absence of public dataset of moving real-world deformable objects, we construct a novel real-world dataset in our study. By using a high-speed camera that can capture up to 480 frames per second, we film a fast moving real-world deformable object. We throw a deformable object from various positions with varying forces and directions that are similar to the behavior of simulated deformable objects we formulated when generating the synthetic dataset. Since we convert our video data into a sequence of 2D point sets, we control the depth value of the object by throwing the object in parallel with the camera at a constant distance.

Data preprocessing We preprocess the video data to obtain the particle positions data that our model can consume

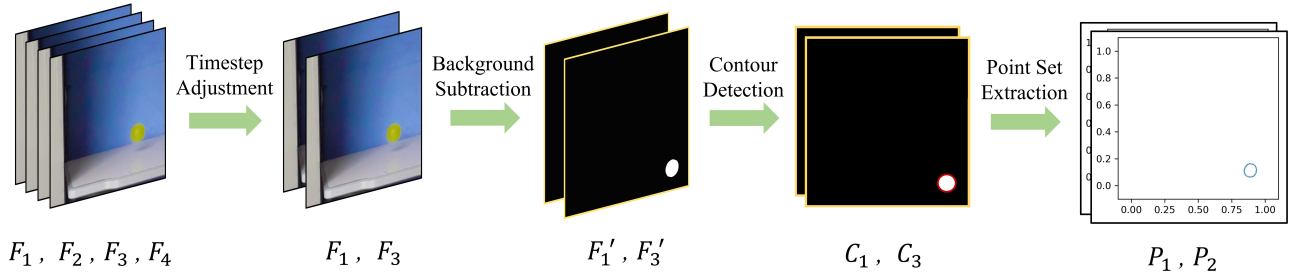


Figure 7: The process of obtaining point set data from video frames. F_i denotes a frame captured from the original video at time i . F'_i denotes a frame with background subtraction at time i . C_i denotes the contour of the object extracted from the frame at time i .

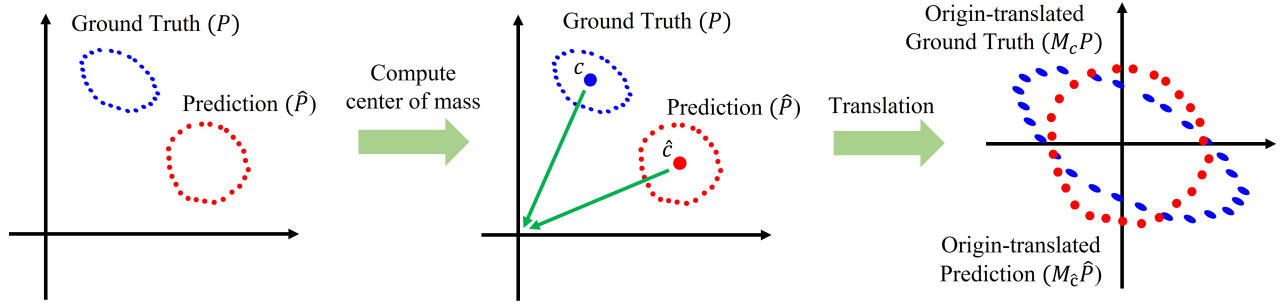


Figure 8: Visualization of the process of computing shape error E_s

as input. As illustrated in Figure 7, we apply a series of operations to the original video frames to obtain the point set P for each time step. The first step is to sample video frames at odd time steps, to adjust the time step of real-world deformable object to be similar to that of the simulated deformable object, that our model was trained on. Then, for each frame, we subtract the background to identify the contour C of the deformable object in the frame. After we obtain the contour of the object, we uniformly divide the contour into n points as described in Figure 6 to obtain the particle positions data P . Although the obtained point sets P_1 and P_2 in Figure 7 represent the states that are originally two time steps away from each other, we define them as point sets with consecutive time steps. Note that we also normalize the position data to be between 0 and 1, by using the relative pixel coordinates with respect to the wall and floor. When we visualize the predicted point sets, we plot the points on the background image by computing its relative pixel coordinate.

B Evaluation

Adoption of shape error As described in Section 4, we use two metrics to evaluate our model – position error(E_p) and shape error(E_s). The purpose of using two metrics for evaluation is to evaluate the prediction accuracy of our model in two different perspectives. As shown in Equation 11, position error is the Chamfer distance between the ground truth point set and predicted point set, which measures the distance between individual particles. In Figure 9,

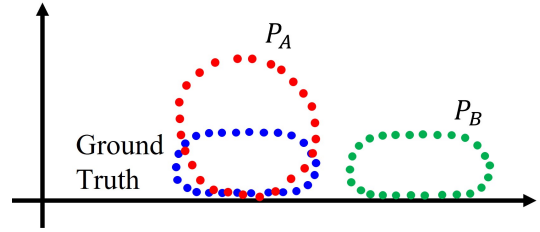


Figure 9: Limitations of using the vanilla Chamfer distance (position error) as a single evaluation metric of the performance of our model

it is clear that P_A is a better prediction of the ground truth than P_B , in terms of position error since the distances between individual particles are much closer than that of P_B . However, it is clear that P_B is a much better prediction of the ground truth in terms of shape. Therefore, using the vanilla Chamfer distance as a single evaluation metric can lead to a false interpretation of the performance of the model in these cases. In order to prevent such behavior, we define our shape error as described in Equation 12.

Computing shape error Although we provide an equation for computing the shape error in Equation 12, we provide an illustration of the process of computing the shape error for better understanding of shape error. As illustrated in Figure 8, we first compute the center of mass c and \hat{c} of each point set P and \hat{P} , respectively. Then, we apply a trans-

lation matrix M_c and $M_{\hat{c}}$ to P and \hat{P} , respectively, to align each point set with respect to the origin. After translating each point set, we then compute the Chamfer distance between these translated point sets to compute the shape error.